

AERODYNAMICS OF BOUNDARY LAYER INGESTING FANS

E. J. Gunn and C. A. Hall

Whittle Laboratory
University of Cambridge
1 JJ Thomson Avenue
Cambridge CB3 0DY, UK
Email: ejg55@cam.ac.uk

ABSTRACT

Boundary Layer Ingesting (BLI) turbofan engines could offer reduced fuel burn compared with podded engines, but the fan stage must be designed to run continuously with severe inlet distortion. This paper aims to explain the fluid dynamics and loss sources in BLI fans running at a cruise condition. High-resolution experimental measurements and full-annulus unsteady CFD have been performed on a low-speed fan rig running with a representative BLI inlet velocity profile. A three-dimensional flow redistribution is observed, leading to an attenuation of the axial velocity non-uniformity upstream of the rotor and to non-uniform swirl and radial angle distributions at rotor inlet. The distorted flow field is shown to create circumferential and radial variations in diffusion factor with a corresponding loss variation around the annulus. Additional loss is generated by an unsteady separation of the casing boundary layer, caused by a localised peak in loading at the rotor tip. Non-uniform swirl and radial angles at rotor exit lead to increased loss in the stator due to the variations in profile loss and corner separation size. An additional CFD calculation of a transonic fan running with the same inlet profile is used to show that BLI leads to wide variations in rotor shock structure, strength and position and hence to loss generation through shock-boundary layer interaction, but otherwise contained the same flow features as the low-speed case. For both fan geometries, BLI was found to reduce the stage efficiency by around 1-2% relative to operation with uniform inlet flow.

INTRODUCTION

The use of Boundary Layer Ingesting (BLI) engines for aircraft propulsion could theoretically enable fuel burn reductions of up to 15% compared with conventional engines [1-3]. In a BLI aircraft the engines are integrated into the fuselage so their intakes capture fluid from the airframe boundary layer. This fluid is re-energised within the fan stage, reducing the

wasted kinetic energy in the aircraft's wake and increasing the propulsive efficiency compared with a podded engine [4].

One of the key technical challenges in BLI is the design of the engine fans. A BLI fan must run continuously with high levels of inlet flow non-uniformity, or 'distortion'. This creates several difficulties for the fan designer, including the need to maintain thrust, efficiency and stability, and to avoid mechanical failure. This paper focuses on the aerodynamics of BLI fans operating at a cruise condition and aims to establish an understanding of how BLI affects the fluid dynamics and loss generation in a fan stage.

There are many proposed BLI aircraft configurations and thus different possible inlet flow fields for fan designers to consider. These range from blended wings with high-bypass engines embedded in ducts [5] to cases where the propulsion is distributed over many smaller fans powered by separate main engines [2]. Modified tube-and-wing configurations are also proposed [1]. In all cases the fans must ingest a radially and circumferentially non-uniform inlet mass flow distribution.

Inlet distortion is found to reduce compressor pressure rise, efficiency and stability margin [6] and to increase blade forcing [7]. These effects can be qualitatively explained by the fact that it is impossible for a rotating blade row to run at its design condition everywhere in the annulus if the inlet flow is circumferentially non-uniform. The severity of the effect depends on both the intensity of the distortion and its lengthscale. Long length-scale distortions, like those encountered in BLI, lead to greater reductions in performance [8] and to increased flow field coupling between adjacent blade rows, inlets and exhausts [9, 10]. Historically most distortion tests were carried out on high hub-to-tip ratio compressors. Recently, full-annulus, unsteady CFD calculations [11, 12] and detailed experiments [13, 14] have shown that distorted flow in fans is highly three-dimensional, with circumferential and radial flow migration upstream of the rotor and wide variations in the flow field both around the annulus and up the span.

Previous studies of fan distortion have generally used idealised inlet velocity profiles, often circumferential square waves. The fluid dynamics involved in mixed circumferential/radial distortions of the type seen with BLI are not currently well understood. This paper aims to gain further insight by testing with a representative aircraft inlet boundary layer profile. The results show that the fan response has important differences to when either radial or circumferential distortion is present in isolation. Choosing a distortion of representative intensity also allows the quantitative impact of BLI on fan pressure rise and efficiency to be determined.

This paper considers two test cases. The first is a purpose-built, low-speed experimental fan rig with a simple geometry which has been tested with a BLI inlet flow field. This fan is the main focus of the paper. The experimental results, along with a full-annulus unsteady CFD calculation of the test point, are used to understand the fluid dynamics and loss sources in the machine. Results are then presented from a CFD calculation of a low pressure ratio, transonic fan running with the same inlet BLI profile. This case is used to remove the low-speed limitation of the earlier results and to understand compressible flow effects within a more realistic BLI engine fan architecture.

TEST CASES

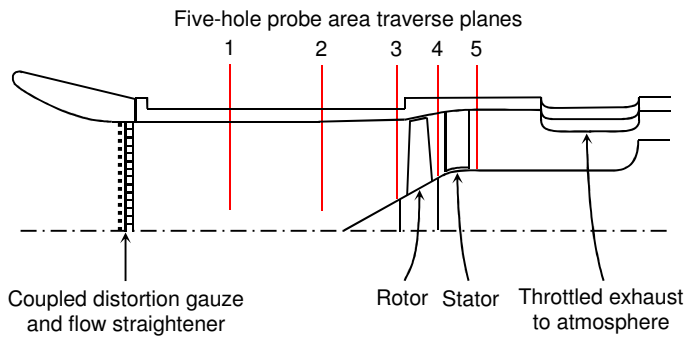
Figure 1 shows the two fan geometries considered in the paper and some relevant parameters are set out in Table 1. The BLI fan rig and the associated experimental methods are described below, followed by the computational approach for both fans.

Experimental Methods

The BLI rig is a low-speed, single-stage fan. The flow field throughout is incompressible. The rig was purpose-built for making fan-distortion interaction measurements but the blading was designed for operation with a clean inlet and no special allowance was made for distortion tolerance. The blades were designed with similar velocity triangles to current civil fans, although since the rig has no compressible flow features and a relatively large tip clearance it cannot be fully representative of an engine fan. A long intake duct allows the rotor to interact freely with the distorted upstream flow field.

Measurements were carried out with a five-hole pressure probe area traverse system at five axial stations. The probe measured the time-averaged stagnation and static pressures and the swirl and radial flow angles. In low-speed machines the 3D velocity field, work input and loss can be calculated from these measurements. The estimated uncertainties were of the order of 0.1% and 0.5% of dynamic head respectively for the pressure fields and 0.5° in flow angle. The area traverse system operates within a 36° sector of the rig; clocking the inlet distortion ten times relative to this sector allowed measurements of the full annulus flow field to be taken. Measurements were taken at 34 radial positions and 1° circumferential intervals at stations 1-4, and 0.5° intervals at station 5. The probe was unable to reach zero radius at stations 1 and 2 but for performance calculations the inlet was taken to be at station 3, where the full flow field was traversed.

**a) Low-speed fan rig ('BLI Rig') – Experiment + CFD
Rig schematic (to scale)**



**b) Transonic research fan ('VITAL Fan') – CFD Only
Computational domain**

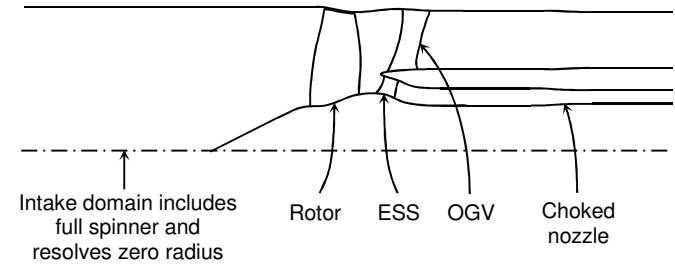


Figure 1: Meridional view of the BLI Rig and computational domain of the VITAL Fan.

	BLI Rig	VITAL Fan
Flow coefficient = V_1/U_{mid}	0.50	0.65
Stage loading coefficient = $\Delta h_0/U_{\text{mid}}^2$	0.47	0.48
Rotor inlet tip M_{rel}	0.13	1.25
Rotor tip Reynolds number	2.0×10^5	2.3×10^6
Rotor inlet hub/tip radius ratio	0.30	0.33
Running tip clearance (% span)	0.50	0.20

Table 1: Design point flow parameters and geometry for the two test case fans.

The inlet boundary layer profile chosen for the rig test was taken from work on the Cambridge-MIT Institute Silent Aircraft [15]. This was a concept design of a blended-wing body aircraft with nine BLI fan stages embedded in S-duct intakes. A computational study and optimisation of the inlet geometry is described in [16]. The calculated duct exit velocity profile at cruise is shown in Fig. 2(a). It contains the key features of most BLI profiles seen in the literature: a smooth velocity variation in the vertical direction covering most of the fan diameter, with a lobe of low-momentum fluid at the bottom generated by secondary flow in the intake duct.

To model this profile in the rig, a distortion gauze was designed and installed in the intake. A 3D printer was used to produce the gauze as a single sheet with a precisely controlled, non-uniform porosity distribution. A simple calculation, detailed in the Appendix, was used to determine the porosity variation necessary to impose the desired profile in the rig. The reproduction of the target velocity profile was verified by traversing the flow field at station 1, upstream of rotor potential flow field. Figures 2(b) and (c) show that the method gives

a good match to the target profile with smooth velocity gradients. The spatial noise in the achieved profiles is repeatable and is caused by the discrete holes of the gauze. The limitation of this gauze method is that it models only the intake mass flux distortion and does not account for the presence of inlet duct secondary flows or distortion of the intake static pressure field, which are beyond the scope of this paper.

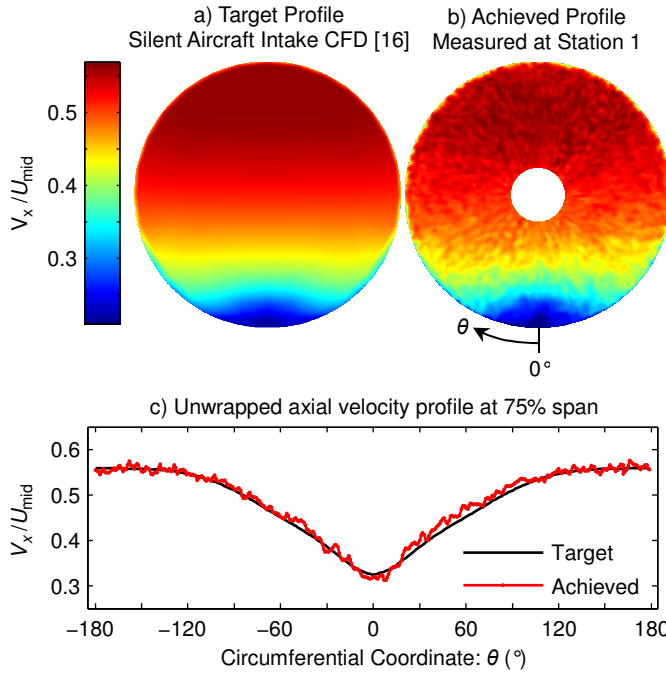


Figure 2: Comparison of the target inlet profile [16] with the measured velocity profile at station 1 in the BLI Rig.

Computational Approach

Full-annulus, unsteady simulations were performed of both the BLI rig and the VITAL fan. The CFD solver used was Turbostream [17], a 3D, unsteady, Reynolds-averaged Navier Stokes solver running on structured multi-block meshes. The solver was run on a graphics processing unit cluster, allowing the full-annulus calculations to be completed in around two weeks each. The one-equation Spalart-Allmaras (SA) turbulence model was used [18]. All meshes were created with PADRAM [19] and were of the multiblock HOH topology with an O-mesh surrounding each blade. Around 2 million nodes were used per rotor blade passage and for both fans the total node count was around 80 million. Other CFD studies of distortion transfer have found good agreement with experiment using the SA model and similar mesh densities [11, 12, 20]. Inlet distortion is generally a long lengthscale problem and therefore it is usually found that no special turbulence modelling or blade row meshes are required. However, it is necessary to model a long domain to allow sufficient space for the fan-distortion interaction. In this case the computational domain extended for 1 diameter upstream and downstream of the rotor. The inlet boundary condition for the BLI rig simulation consisted of the measured stagnation pressure profile at station 1, where the flow was confirmed to be axial with uniform static pressure. For the transonic simulation this stagnation pressure profile was scaled to produce the same non-dimensional velocity profile at the appropriate inlet mass flow rate.

The VITAL fan [21] was chosen for the transonic test case because it was designed to demonstrate 2020-2030 timeframe fan technology for high-bypass, 3-spool engines, with a rotor pressure ratio of about 1.45. This makes it representative of a fan that could be used in a practical BLI application. Both the bypass and core engine streams were modelled, including the Outlet Guide Vane (OGV) and Engine Section Stator (ESS) blade rows as shown in Fig. 1(b).

For the core exit boundary condition it was necessary to mimic the presence of an intermediate pressure compressor (IPC) downstream of the ESS, because its pressure field would alter the response to the distortion. This was achieved by placing a choked nozzle just downstream of the ESS, with an area ratio set to choke the flow at the core engine design point flow rate. A choked nozzle has a vertical pressure rise versus mass flow characteristic curve. This is approximately representative of the IPC which has a much greater pressure ratio than the fan stage. A static pressure exit boundary condition with radial equilibrium was imposed on the bypass stream.

Operating Point and Overall Performance

The fan operating points were set so the total mass flow rate with BLI matched the design point flow rate in clean flow. The resulting operating point is shown for the BLI rig in Fig. 3. Table 2 also quantifies the effect of BLI on efficiency for both fans relative to their design points. For the BLI rig, experimental values were mass-averaged from the full-annulus area traverse measurements. The CFD values were evaluated at axial planes corresponding to the real experimental stations. For the VITAL fan, averaging planes were chosen to be at similar distances from the blade rows to those shown in the BLI rig schematic. Stage exit values for the VITAL fan were mass-averaged across both the core and bypass streams.

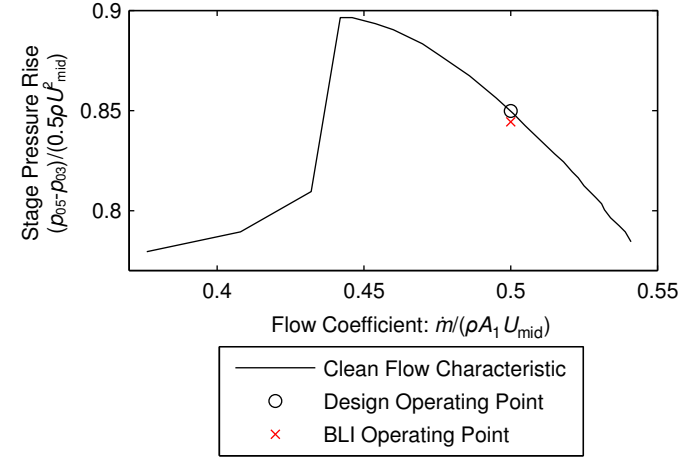


Figure 3: Measured clean flow characteristic for the BLI Rig showing the operating point with BLI inlet flow.

	Rotor	Stage
BLI Rig (EXP)	-0.6%	-0.9%
BLI Rig (CFD)	-0.9%	-1.4%
VITAL Fan (CFD)	-1.0%	-1.6%

Table 2: Measured and predicted effect of BLI on fan efficiency relative to values at the design point.

For both fans the reduction in pressure rise was small compared with the reduction in efficiency. This is because BLI increases the stage loading. The resulting increase in rotor work input almost offsets the reduction in pressure rise due to the higher loss. Loss increases in both the rotor and stator, but experiment and CFD both show that BLI is more detrimental to the rotor. The reasons are discussed later in the stator flow field section. The overall stage efficiency drop of order 1% for both fans is an encouraging result. An important caveat is that the efficiency penalty will depend on the particular BLI inlet flow pattern, but values of order 1% have also been published for a different fan and intake system [22].

THREE-DIMENSIONAL FLOW REDISTRIBUTION

Figure 4 shows a conceptual picture of the flow field development through a BLI fan stage. Mass is continually redistributed through the machine because the rotor imparts a non-axisymmetric work distribution in response to the distorted inlet flow. Compared with the design condition, the flow field with BLI is highly three-dimensional and has greater coupling between the spinner, rotor and stator. These features will be shown to have a direct impact on the loss generation. This section explains the overall physics of the flow redistribution before the blade row performance is considered in detail later.

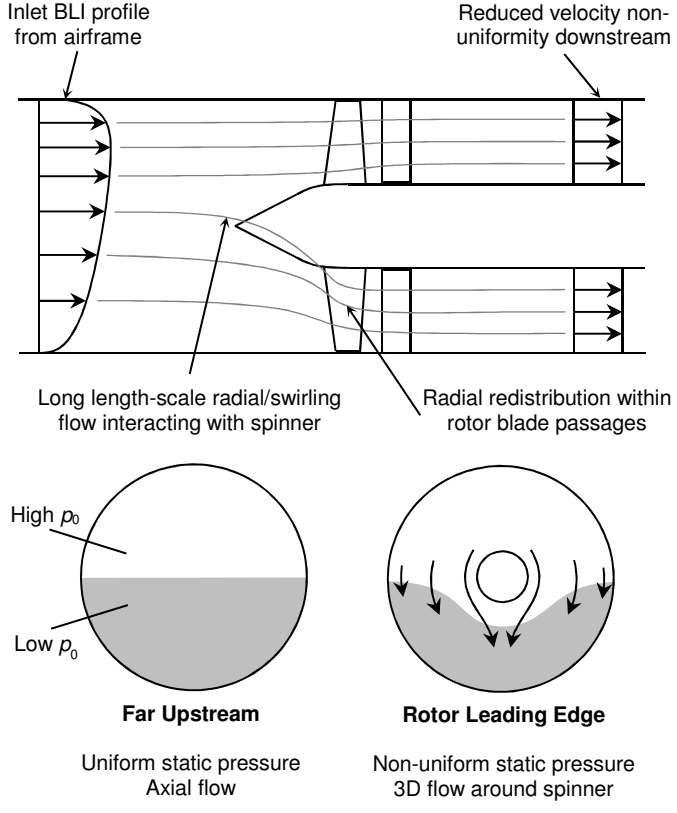


Figure 4: Sketch of the 3D flow redistribution in a BLI fan.

On the left of Fig. 4, well upstream of the rotor, the inlet boundary layer profile is convected to the fan from the airframe. It was found that at distances above about one casing diameter upstream of the rotor, the flow is essentially decoupled from the fan and the static pressure is almost uniform. As the flow approaches the rotor, a non-uniform static pressure

field is induced, shown in Fig. 5(b). Low static pressure is induced in regions of slower-moving flow, as these regions experience higher work input in the rotor. The resulting pressure gradients drive a redistribution of mass. Fluid migrates from the upper half of the annulus towards the bottom. The flow angles in Fig. 6 show that the redistribution is three-dimensional – a consequence of the low hub-to-tip ratio. High-momentum fluid is driven around the spinner, creating counter-swirling (B) and co-swirling (C) regions of flow. This fluid then migrates radially up the span in the bottom half of the annulus (D). The redistribution causes the streamtube in the bottom half of the annulus to contract, as can be seen in Fig. 5(a). Upstream of the rotor the stagnation pressure field convects along streamlines. The rotor inlet profile therefore resembles the upstream velocity profile from Fig. 2, but the yellow contour bulges downwards near the spinner (A), indicating flow migration around the hub as sketched in Fig. 4.

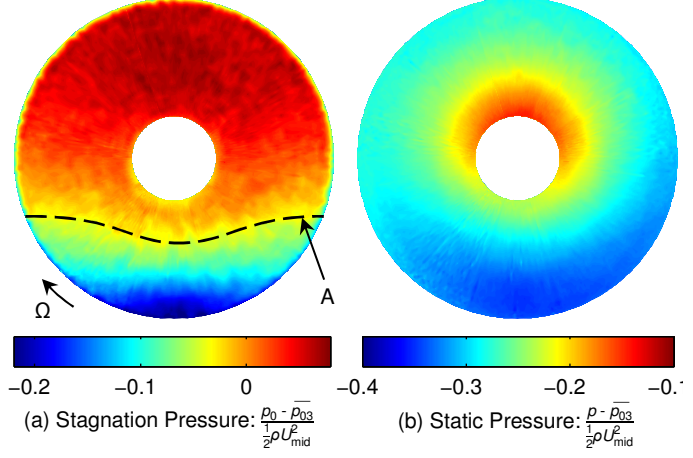


Figure 5: Measured stagnation and static pressure fields at station 3 in the BLI Rig.

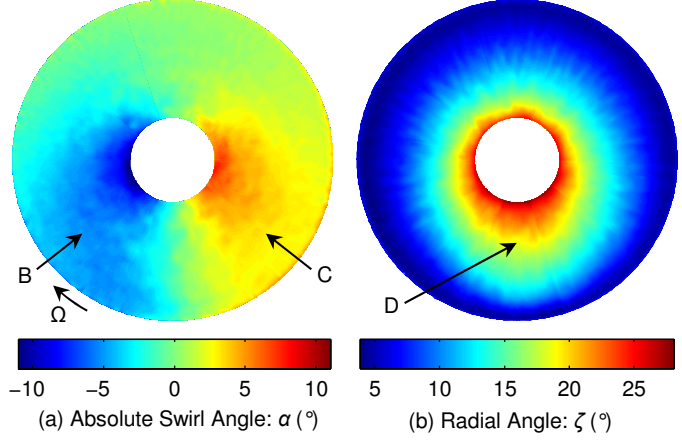


Figure 6: Measured flow angles at station 3 in the BLI Rig.

Figure 7 shows how this redistribution leads to an attenuation of the axial velocity distortion through the machine (in the low-speed rig, axial velocity is directly proportional to mass flux). At all radial heights, the axial velocity distortion decreases between stations 2 and 3. The original BLI profile featured a greater axial velocity deficit towards the casing, and the curves at 75% span also show greater attenuation of the axial velocity deficit towards the casing.

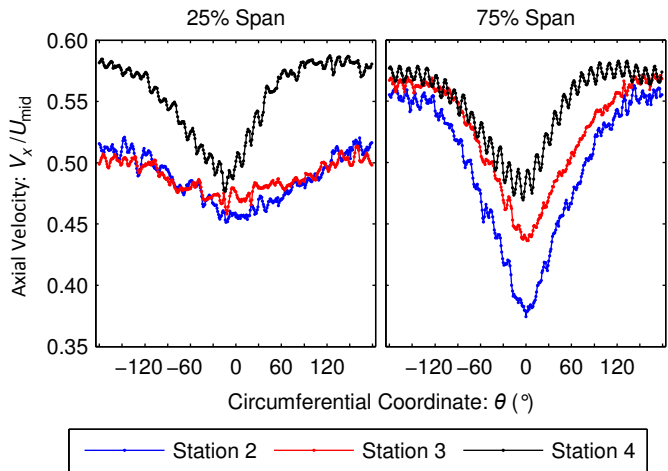


Figure 7: Measured development of the axial velocity distortion through the BLI Rig.

Flow redistribution continues within the rotor passages but circumferential redistribution is blocked over length-scales greater than the blade pitch and the amount of mass in each passage is fixed. The redistribution is therefore purely radial and this changes the behaviour compared with upstream. Figure 7 shows that at 75% span, the circumferential axial velocity distortion is further decreased between stations 3 and 4. On the other hand, at 25% span the circumferential component of distortion is increased within the rotor. This is caused by a radial flow of mass from the hub to the casing within the rotor passages, which can be seen in Fig. 8. High values of radial velocity in the rotor passages near $\theta = 0^\circ$, in the centre of the plot, indicate that in this region the rate of spanwise migration of mass is increased compared with elsewhere in the annulus. Figure 8 also shows that this radial flow is maximised in the vicinity of the rotor leading edge but it can be seen to persist throughout the passage and downstream of the trailing edge, leading to a non-uniform radial angle distribution in the stator. The increase in circumferential distortion near the hub has not been observed in previous tests with purely circumferential distortions and is a consequence of the mixed distortion that occurs with BLI. Later in the paper the increased distortion at the hub is shown to lead directly to flow separations in the stator row. The radial flow also has a direct impact on loss generation in the rotor by modifying the diffusion through the blade passages, as explained in the following section.

Both black curves in Fig. 7 have almost the same shape. This indicates that the mass flow distribution at rotor exit is more uniform in the radial direction than it is in the circumferential direction. This is shown more clearly in Fig. 9 which plots several radial distributions of axial velocity at rotor inlet and exit. At station 3 the axial velocity profile at 0° has a different shape to the other curves, with a deficit near the casing but almost the same value at the hub. At station 4 the various profiles have the same shape but are offset on the horizontal axis, indicating radial uniformity but circumferential non-uniformity. This supports the conclusion that the radial component of mass flow distortion is eliminated within the rotor through the radial flow mechanism described above.

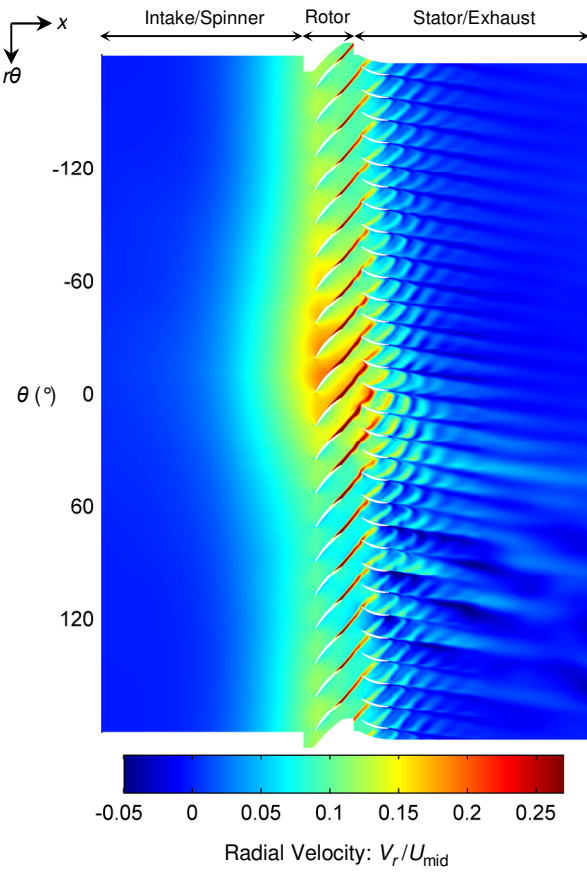


Figure 8: Computed radial velocity distribution at mid-span in the BLI Rig.

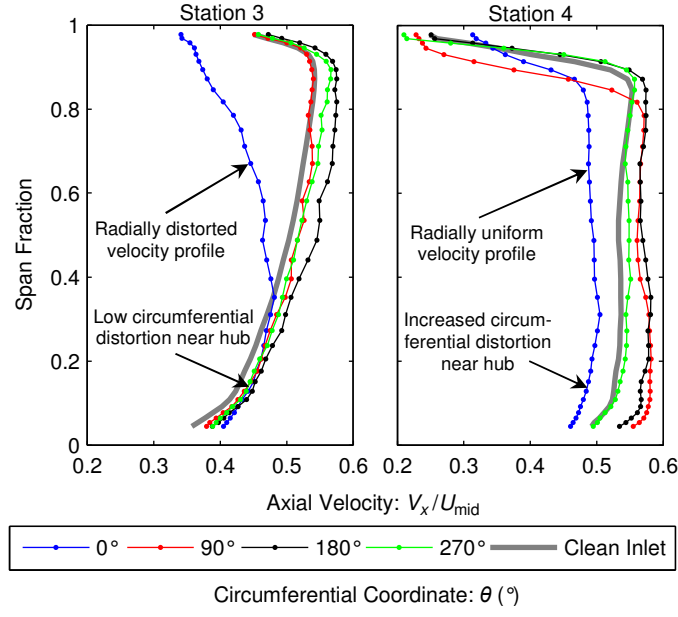


Figure 9: Measured rotor inlet and exit axial velocity distributions in the BLI Rig at four circumferential positions with BLI inlet flow. Clean inlet flow profiles shown in grey.

ROTOR FLOW FIELD

The flow redistribution acts to reduce the mass flow non-uniformity at rotor inlet compared with far upstream. Nevertheless, the axial velocity distribution departs from the design condition and the 3D flow leads to varying swirl and radial angle distribution. Many aspects of the rotor performance can be understood by considering the resulting leading edge incidence variation, which is shown in Fig. 10 with a breakdown of the underlying axial velocity and swirl profiles. Incidence is defined as positive when the stagnation point lies on the blade pressure surface.

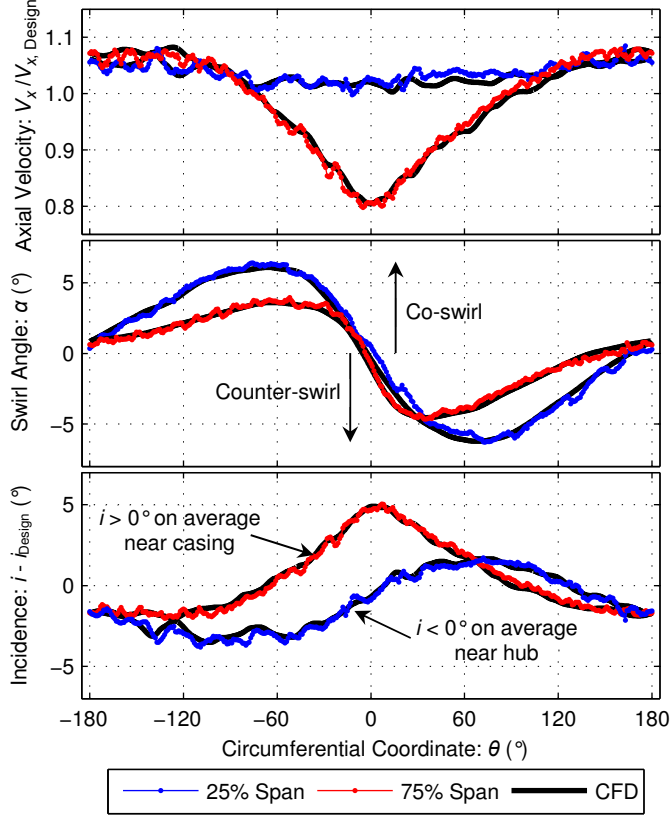


Figure 10: Measured and computed axial velocity, swirl and incidence variations at station 3 in the BLI Rig.

Near the hub (blue curves) there are regions of intense co-swirl and counter-swirl where the flow migrates around the spinner. The flow is at negative incidence onto the rotor in regions of co-swirl and vice-versa. There is little axial velocity non-uniformity near the hub so the incidence variation is created mainly by this swirl distribution. However, Fig. 10 also shows that the blue axial velocity curve is everywhere above the design value. On average, the rotor hub sections therefore run at a more negative incidence than the design intent. Generally the converse is true near the casing (red curves). Here there is less swirl distortion but a large axial velocity deficit. This creates an incidence variation that is positive on average and has a peak near 0° where the velocity deficit is greatest. The most important result from Fig. 10 is that the rotor does not operate at its design condition anywhere in the annulus.

Figure 11 compares the full-annulus incidence distribution with the stagnation enthalpy field at rotor exit. BLI does not cause any variation in the rotor inlet stagnation temperature, so

the stagnation enthalpy field at station 3 is uniform and Fig. 11(b) directly shows the rotor work input. Regions of low axial velocity or counter-swirl, and hence positive incidence, experience greater flow turning through the rotor and therefore receive high work input relative to regions of negative incidence. This is confirmed by comparison of Figs. 11(a) and (b). However, the radial flow redistribution changes the 1D diffusion and turning through the rotor blade passages, so the work input is not solely a function of the inlet incidence. Compared with the design stage loading value of 0.47, with BLI the loading varies circumferentially by up to 20%. This work variation is not, in itself, a problem. It is the mechanism by which the fan recovers the stagnation pressure deficit in the boundary layer and produces a more uniform wake downstream of the aircraft. The problem is the associated variation in loss and hence the reduction in rotor efficiency.

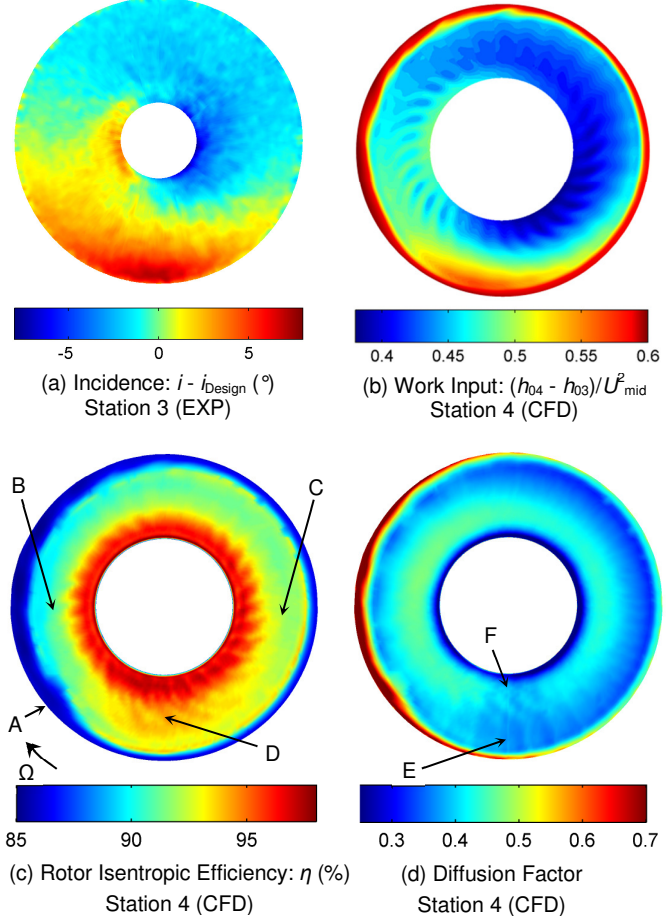


Figure 11: Rotor incidence, work, loss and diffusion variations in the BLI Rig.

Because the inlet stagnation pressure is non-uniform, to obtain a detailed breakdown of the rotor loss it is necessary to track streamlines between rotor inlet and exit. To avoid the need for time-accurate particle tracking, the rotor flow field was time-averaged in the absolute frame of reference using a method described in [11]. The full flow field between stations 3 and 4 was extracted at 360 timesteps over one rotor revolution. At each timestep, and at 60 axial locations, this flow field was interpolated onto a stationary, bladeless grid which was then time-averaged. Standard streamlining procedures were

then used to match particles at station 4 to their inlet positions at station 3. The method was verified by checking for continuity and conservation of rothalpy through the streamtubes identified in this process. Note that the average circumferential particle displacement between stations 3 and 4 was found to be around 10°. This is small compared to the distortion lengthscale so circumferential phase shift can be neglected when comparing the rotor inlet and exit flow fields in any of the plots in the paper.

Figures 11(c) and (d) show contours of rotor isentropic efficiency and Lieblein's diffusion factor (DF) [23] at station 4, both evaluated along streamlines traced from station 3. The diffusion factor was calculated using rotor inlet and exit relative velocities, with terms accounting for both bulk diffusion and flow turning respectively:

$$DF = 1 - \frac{V_{4,\text{rel}}}{V_{3,\text{rel}}} + \frac{1}{2} \frac{|V_{\theta 4,\text{rel}} - V_{\theta 3,\text{rel}}|}{V_{3,\text{rel}}} s \quad (1)$$

Below about 80% span the efficiency varies smoothly around the annulus. Above 80% span the variation is not smooth and is dominated by a thick band of high-loss fluid at the casing (A); this tip flow is discussed separately below. At all radial heights, minimum efficiency generally occurs around $\theta = 90^\circ$ (B) and it increases moving clockwise to a maximum near $\theta = 0^\circ$ (D). Figure 11(d) shows that over most of the span the diffusion factor is maximised near B, explaining the high loss. This is caused by the high-velocity counter-swirling flow in this region which raises both the bulk diffusion and the turning terms in Eq. (1). Moving clockwise the swirl angle becomes more negative, developing into co-swirl in the right half of the annulus. This decreases both the diffusion terms and Fig. 11(d) shows the efficiency rising as a result. Between B and C this increase in efficiency also follows trends of decreasing incidence and rotor work input.

The high-efficiency region at D is counter-intuitive because much of this area is at high positive incidence and receives high work input from the rotor. However, Fig. 11(d) shows that this is possible because despite the high flow turning, over most of the span the diffusion factor is low compared with the rest of the annulus. This is caused by the radial flow in the rotor that was identified in the previous section. Figures 7 and 9 show that this radial flow increases the axial velocity through the rotor at high span fractions near $\theta = 0^\circ$. This acceleration reduces the bulk diffusion through the blade passage and the total diffusion factor around E remains low despite the high flow turning. Conversely, at F the radial redistribution has the opposite effect and the axial velocity distortion increases, raising the bulk diffusion term. However the total diffusion factor remains low here because the negative incidence near the hub reduces the turning term instead. The overall effect of this radial flow is to decouple the diffusion factor from the incidence and work variations. It is therefore the diffusion factor, evaluated in a manner that accounts for the 3D flow field, which should be used to fully understand the loss distribution in BLI fans.

Figure 12 shows the time-averaged and instantaneous axial velocity fields just downstream of the rotor. They reveal that the high-loss band at A (Fig. 11(c)) is caused by a flow separation at the casing. In the time-averaged flow field, Fig. 12(a),

and moving clockwise with the rotor, a band of low-momentum fluid around the casing thickens just before bottom dead centre (G) as the tip sees increasing positive incidence (cf. Fig. 11 (a)). Just after the positive incidence peak the thickness of this band is maximised (H) but the axial velocity deficit further increases to (I). The tip performance then gradually improves and between points J and G the tip flow is similar to that seen without BLI. Figure 12(b) shows that the tip separation is unsteady and consists of discrete lumps of low-momentum fluid (K). These regions have about the same width as the blade pitch and are created by a separation of the casing boundary layer inside the rotor passages. Table 1 shows that the BLI rig runs with a larger tip clearance than real engine fans. When run with the same inlet flow field, the VITAL fan had a less severe response at the tip (shown further below), although its casing boundary layer did show similar trends to those in Fig. 12. The goal here is not therefore to claim that the behaviour of the BLI rig rotor tip is fully representative of BLI fans in general. However, the effect is relevant because ducted BLI fans will run with thicker casing boundary layers than podded fans. The fan interaction with the main airframe boundary layer should not be the only concern for BLI intake and fan designers. The casing boundary layer and tip clearance are also important in dictating performance.

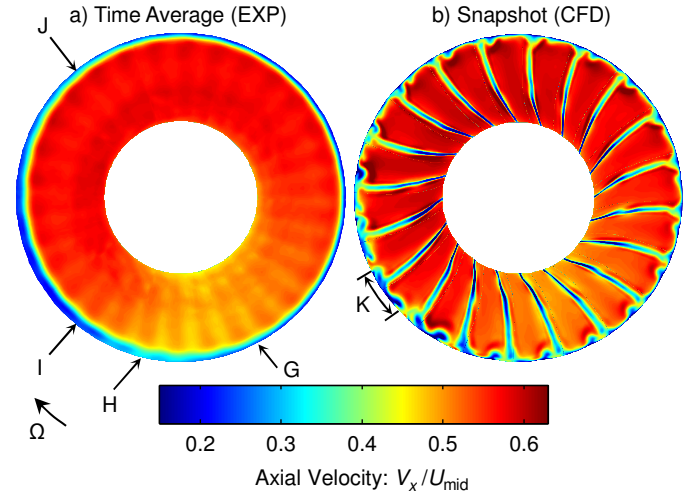


Figure 12: Time-averaged and instantaneous axial velocity distributions at station 4 in the BLI Rig.

The main finding is that the additional loss generated in BLI fan rotors is due to a combination of 1) a relatively small and smooth radial and circumferential variation in rotor efficiency, and 2) localised, non-linear effects like the unsteady flow separation near the tip. It has also been shown that this loss distribution can be explained by combining an understanding of the 3D flow redistribution with some simple diffusion factor arguments.

STATOR FLOW FIELD

The swirl and radial angle distributions in Fig. 13 show that the stator inlet flow field is distorted throughout the annulus. Therefore, similarly to the rotor, every stator blade operates at an off-design condition. The distortion had little effect on the relative flow angle at rotor exit, generally changing it by 3° or less. The swirl angle variation presented to the stator

is instead caused by the propagation of the mass flow distortion through the rotor, as shown by the velocity triangle sketch in Fig. 14. Regions of low axial velocity at rotor exit correspond to regions of high flow angle onto the stator and vice versa (cf. Figs. 7 and 13). Swirl angle distortion leads to varying incidence onto the stator blade sections, while the radial angle distortion effectively creates positive incidence in a meridional plane relative to the hub endwall.

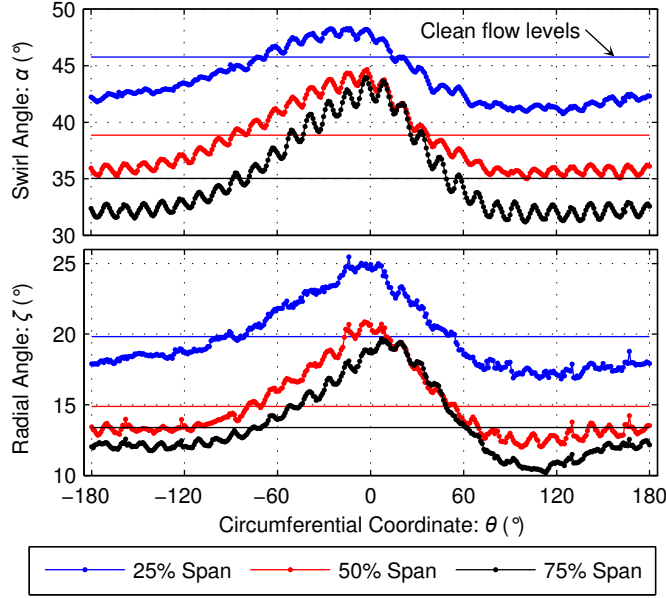


Figure 13: Measured flow angles at station 4 in the BLI Rig. Coloured horizontal lines show clean flow values.

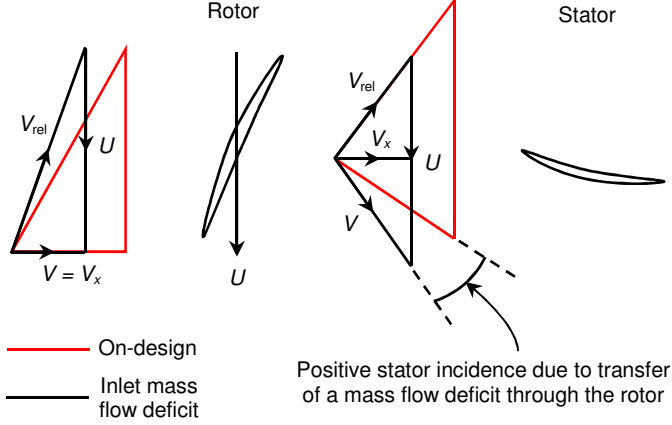


Figure 14: Stator blade incidence variation due to a mass flow deficit passing through the rotor.

The effect on the stator exit flow field is shown in Fig. 15. Compared with the design condition in Fig. 15(a), in BLI operation there are variations in both the wake thicknesses and in the size of the corner separations. There are two groups of large separations at the hub (A) and tip (B). The hub separations are caused by a combination of high swirl and radial flow angles. Note that at rotor inlet, the mass flow distribution near the hub was close to uniform. The hub separations at (A) are a direct result of the radial flow redistribution within the rotor blade passages, which was shown to increase the mass flow distortion near the hub at rotor exit. The tip separations

are in turn caused by the rotor tip separation just upstream, which creates a band of fluid around the casing at stator inlet with low axial velocity and high swirl angle. As well as these non-linear effects, the wake thickness varies smoothly around the annulus following the swirl angle profiles in Fig. 13.

Further comparison of Figs. 15(a) and (b) shows that some of the stator blades have lower loss with BLI and many of the hub separations are actually reduced in size (C). This is caused by the converse of the argument in Fig. 14. The axial velocity in these regions is higher than the design point value, leading to reduced flow turning and diffusion in the stator. This partially, but not totally, offsets the increased loss elsewhere and helps to explain why BLI was found to be more detrimental to the rotor than the stator in Table 2.

The key result from this section is the importance of the rotor exit axial velocity distribution in setting the stator inlet flow field. The stator performance is therefore governed not just by the blade row design itself, but also the degree to which the upstream flow field is redistributed by the rotor.

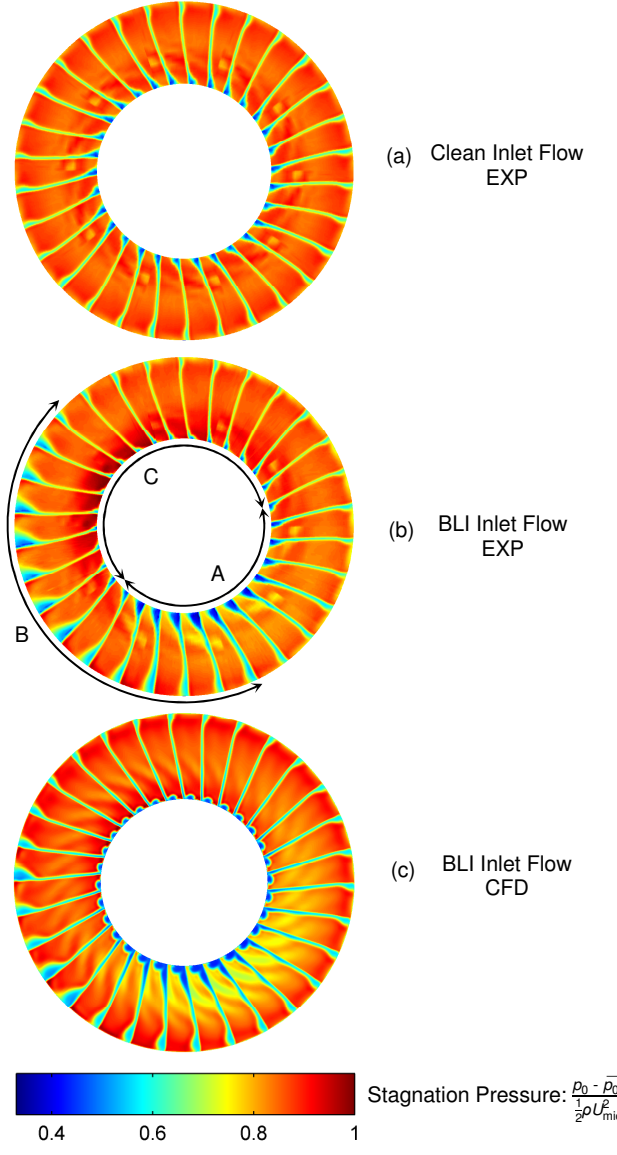


Figure 15: Effect of BLI on the stator exit stagnation pressure field in the BLI Rig.

TRANSONIC FAN TEST CASE

The main differences between the VITAL fan and the BLI rig were the Mach number, rotor tip clearance and the stator architecture. These differences were found to modify the detail, but not the general principles, of the response to the BLI inlet flow. This section uses both the similarities and differences between the fans to develop the understanding further and then explains the effects of transonic flow.

Comparison With the BLI Rig

Qualitatively, the time-averaged flow field upstream of the rotor was found to be similar to that in the BLI rig, as was the flow redistribution through the stage. Neither is significantly affected by compressibility. This can be seen in Fig. 16, which shows that the 3D flow field around the spinner contains the same swirling and radial flow features as Fig. 6. However, it also shows that there are numerical differences in the intensity of the redistribution. This is to be expected from the fact that the fans have differently sloped characteristic curves, so the induced static pressure distortion has a different intensity in the two machines. In addition, a radial redistribution within the rotor was identified and found to be similar to that shown in Fig. 8.

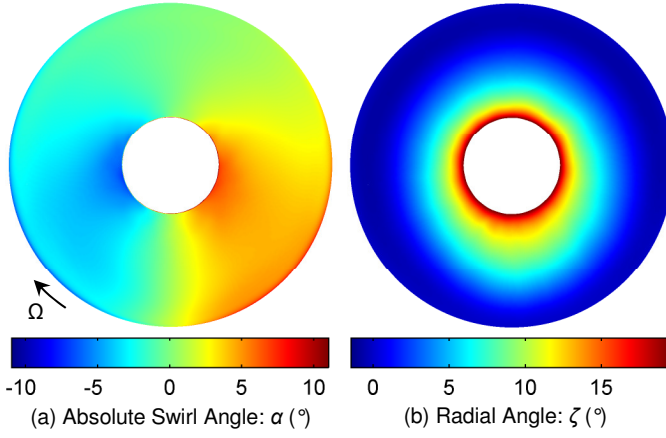


Figure 16: Time-averaged flow angles just upstream of the rotor leading edge in the VITAL fan with BLI inlet flow.

Figure 17 shows the effect of BLI on entropy generation in the VITAL fan. A snapshot of the rotor wakes is shown in Fig. 17(a). As with the BLI rig, over most of the span the entropy generated in the rotor blade boundary layers varies smoothly around the annulus due to the changing variation in diffusion (the entropy distribution visible outside the wakes is convected from upstream). A group of flow separations (A) can be seen both on the hub endwall and extending up to around 20% span. These are caused by shock-induced boundary layer separation, discussed further below. Increased tip loss is also observed around (B). This occurs in the same region as the increased tip loss in the BLI rig, but here the mechanism for the loss is shock-boundary layer interaction.

The casing boundary layer thickens in region (B) but unlike in Fig. 12 it does not fully separate, for two reasons. Firstly, the tip flow field in Fig. 12 is known to be sensitive to tip clearance, as it was found that an accurate measurement of the rig clearance was required to achieve a good match with the CFD. Since the VITAL fan has less than half the clearance gap

size of the BLI rig, an improved tip flow would be expected. Secondly, the BLI rig has a simple, uniform work distribution up the span. Engine fans usually have a more complex work distribution where the tip is unloaded relative to midspan [24] and this was the case in the VITAL fan. The VITAL rotor tip therefore has a lower design-point loading than the BLI rig, leading to reduced sensitivity and a more 2D response when BLI is applied. However, note that despite these differences Table 2 showed that the solver predicted similar efficiency penalties for both rotors.

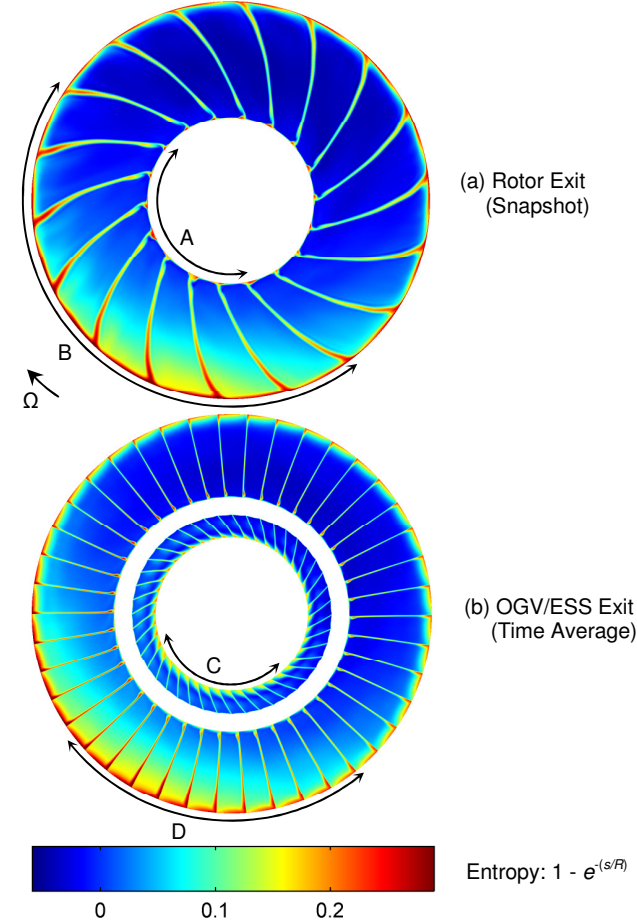


Figure 17: Entropy distributions downstream of the rotor and OGV/ESS in the VITAL fan with BLI inlet flow.

Figure 17(b) shows that away from the endwalls, the OGV/ESS wake thickness varies circumferentially in a similar manner to those in Fig. 15, for the same reasons. The main differences are due to the core/bypass split. The effect of the swirling and radial flows near the hub is mainly seen in the core flow, where the ESS hub corner separation size varies. A group of large hub separations (C) is seen in a similar location to the BLI rig, in places occupying the lower third of the blade passage. The OGV tip is slightly less detrimentally affected by BLI in the VITAL fan because the upstream unsteady flow at the rotor tip is less pronounced. Flow separations near the OGV tip do occur nevertheless (D), but they are more two-dimensional and the corner separations are less significant.

Transonic Flow Effects

In a transonic machine the time-averaged rotor inlet flow field can still be understood using the variations shown in Fig. 10. However, the non-uniform flow conditions lead to a variation in rotor inlet Mach number. At high span fractions the non-uniform diffusion in the rotor is achieved through a non-uniform shock structure, as shown in Fig. 18. In the counter-swirling portion of the annulus (0° to $+180^\circ$), the relative Mach number is greater than the design intent which causes the leading edge and passage shocks to strengthen, merge, and move upstream. The merged normal shock standing upstream of the rotor at E would usually only be seen in a fan running at a near-stall condition. The high pressure gradient through these normal shocks thickens the suction surface boundary layer and produces the thick, high-loss wakes at the tip in Fig. 17 (a). On the opposite side of the annulus where the flow is co-swirling, passage F shows a fully choked structure with a well-swallowed passage shock. In this region the increased loss is instead generated by thickening of the pressure surface boundary layer.

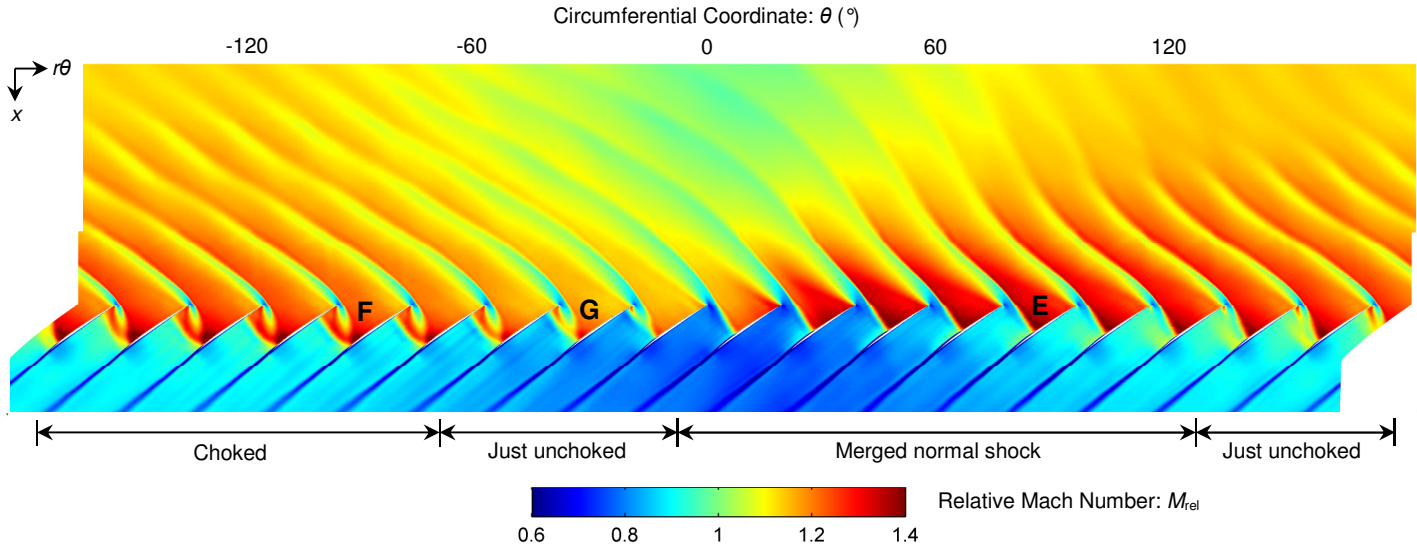


Figure 18: Relative Mach number distribution in the VITAL fan at 90% span with BLI inlet flow.

Figure 19 quantifies these effects. The shape of the curves also proves that the shock structure is largely dictated by the swirl distortion imposed by the upstream flow redistribution in Fig. 10. The relative Mach number varies by around 16% circumferentially near the tip and the passage shock strengthens and moves upstream by 30% of chord as the blades pass from co-swirling flow at F to counter-swirling flow at E. Within this range of Mach number, averaging around 1.25, the entropy creation associated with the shocks themselves is likely to be relatively small [25] and the loss is instead generated indirectly through interaction with the blade and endwall boundary layers as described above. To the authors' knowledge, a detailed study of the aeromechanical consequences of such a wide variation in shock location has not yet been carried out and it is beyond the scope of this paper, but should form the basis of future work.

Figure 19 also reveals that 3 passages near E have supersonic inlet flow over the full blade span down to the hub endwall. This is caused by a combination of the high axial veloci-

ty at low span fractions with the counter-swirl around the spinner (Fig. 10), both of which lead to high relative Mach number at the hub. The resulting shock structure is shown in Fig. 20. The main shock on blade E maintains a relatively constant sweep angle down the span and at the hub the shock lies just downstream of the leading edge. The static pressure rise across this hub shock is comparable to that observed in the passage shock at the tip with the fan running at its design point. In common with most fans, the VITAL rotor hub sections are thick and highly cambered, having not been designed for supersonic inlet flow. The result is the suction surface boundary layer is thickened immediately downstream of the LE and subsequently separates at the point of maximum curvature around mid-chord, leading to the separated wakes observed at A in Fig. 17 (a). Comparison of E and F in Fig. 20 also shows that the shock sweep angle varies circumferentially; the shock at E is relatively unswept compared to that at F, which is more backswept and closer to the design intent. This implies a greater Mach number normal to the shock in the meridional plane as well as the blade-to-blade plane, which fur-

ther contributes to the increased pressure gradient applied to the blade boundary layer.

In summary, with BLI the entire range of possible fan shock structures is present simultaneously at a single overall operating point. This concept has been noted throughout the paper, but the shock structure variation is the most graphic illustration of how BLI leads to off-design operation everywhere in the annulus. The design shock structure in a transonic fan typically features partially merged LE and passage shocks at the tip, with the passage just unchoked [26]. Figure 18 shows that this design intent is unachievable in a BLI fan; in fact only one of the passages (G) contains a shock structure that resembles the design intent. However, it has also been shown that although these effects change some details of the loss variation, particularly at the hub, overall it is still explained by the earlier diffusion factor argument and it is not a direct consequence of the compressible flow features.

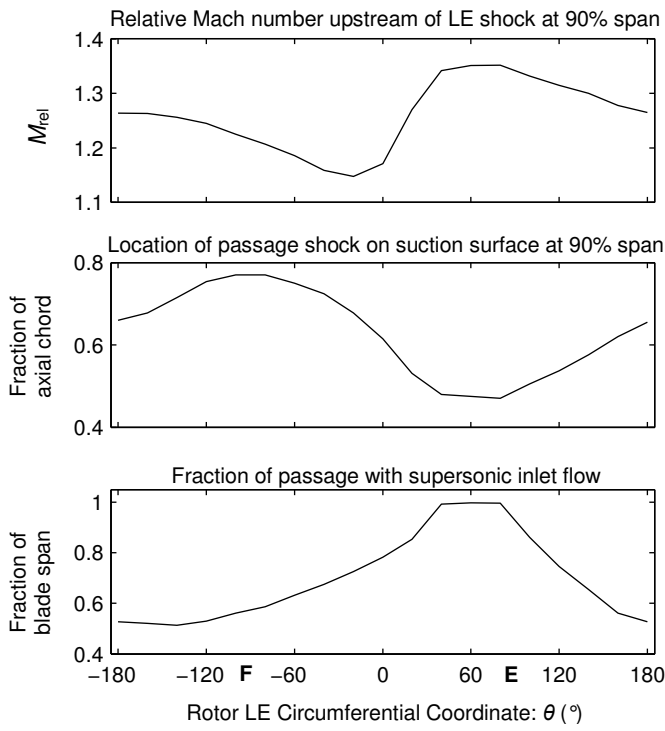


Figure 19: Variation of shock strength, location and spanwise extent in the VITAL fan with BLI inlet flow.

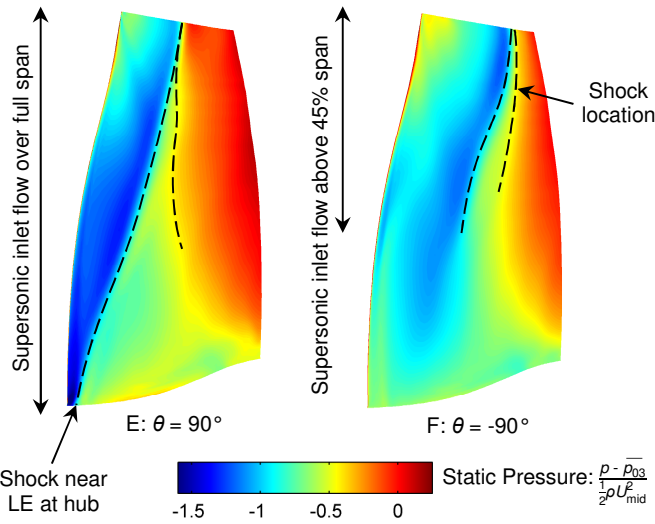


Figure 20: Instantaneous static pressure distributions on the suction surfaces of two rotors in the VITAL fan running with BLI inlet flow.

CONCLUSIONS

1. BLI leads to a three-dimensional redistribution of mass throughout the fan stage. In both test cases, swirling and radial flows were observed upstream of the rotor leading to non-uniform rotor incidence. The mixed radial/circumferential distortion was shown to also cause a radial flow migration within the rotor blade passages.

2. For both test cases, the stage isentropic efficiency penalty due to BLI was found to be around 1-2% relative to operation with a clean inlet. Experiment and CFD agree that

around 2/3 of the additional loss is generated in the rotor and 1/3 in the stator.

3. The additional loss generated in a BLI fan rotor can be broadly broken into two categories:

- A smooth circumferential and radial variation in rotor efficiency due to the non-uniform diffusion through the rotor passages. This component of loss is partly an unavoidable consequence of having inlet flow distortion.
- Non-linear and unsteady effects caused by localised peaks in loading (eg. the separation of the casing boundary layer in the BLI rig).

4. It has been shown that the loss distribution in a BLI fan rotor can be explained using the rotor diffusion factor variation and by understanding the 3D flow field. It has also been shown that the 3D flow features can locally decouple the diffusion factor from the incidence and work variations.

5. The loss generated by the casing boundary layer separation in the BLI rig highlighted the importance of the intake boundary layer and tip clearance, as well as the interaction with the main airframe boundary layer.

6. Non-axisymmetric swirl and radial angle distributions at rotor exit lead to a corresponding pattern of non-axisymmetric corner separations in the stator, and to a circumferential variation in profile loss. The stator inlet flow angles depend on the axial velocity distribution at rotor exit and therefore are determined by the propagation of the BLI velocity profile through the rotor.

7. CFD of the VITAL transonic fan has shown that compressible flow features alter the detail, but not the principles, of fan response to BLI. The loss distribution can still be explained using the understanding of the inlet flow field and diffusion variations developed from the low-speed test.

8. In the transonic fan, the rotor inlet flow non-uniformity creates circumferential and radial variations in relative Mach number. Shock strength, size and position all vary markedly around the annulus; with some passages containing swallowed passage shocks and others containing merged normal shocks. This leads to loss generation through shock-boundary layer interaction and/or separation.

ACKNOWLEDGMENTS

The authors are grateful to Rolls-Royce plc. for funding this work and for permission to publish the results. The authors are also indebted to a large team at Rolls-Royce for their insight into the work, coordinated by Lorenzo Raffaelli and including Adam Bagnall, Gabriel Gonzalez-Gutierrez, Paul Hield, Anthony Parry, Andrew Rolt, Christopher Sheaf, Rory Stieger and John Whurr. Nigel Smith and Qi Qi are also acknowledged for providing the VITAL fan geometry. At the Whittle Laboratory, Graham Pullan, Tobias Brandvik and John Denton are gratefully acknowledged for making the Turbostream solver available to this project; James Taylor and Mike Shaw for assistance with the CFD post-processing methods; and Colin Bullman for supporting the experimental rig tests. Nick Cumpsty and Tony Strazisar are also thanked for their comments on early versions of this work.

NOMENCLATURE

Symbols

<i>c</i>	Blade chord
<i>h</i>	Enthalpy
<i>i</i>	Incidence angle
<i>p</i>	Pressure
<i>r</i>	Radial coordinate
<i>s</i>	Entropy, blade pitch
<i>M</i>	Mach number
<i>U</i>	Rotor blade speed
<i>V</i>	Velocity
<i>x</i>	Axial coordinate
<i>a</i>	Absolute swirl flow angle
ζ	Radial flow angle
η	Isentropic efficiency
Ω	Rotor shaft speed
θ	Circumferential coordinate
ρ	Density

Abbreviations

BLI	Boundary Layer Ingestion
CFD	Computational Fluid Dynamics
ESS	Engine Section Stator
EXP	Experiment
LE	Leading Edge
OGV	Outlet Guide Vane
TE	Trailing Edge
VITAL	EnVIronmenTALLY Friendly Aeroengine

Subscripts

0	Stagnation quantity
1	Value just downstream of gauze
2	Value near spinner tip
3	Value at rotor inlet
4	Value at rotor exit
5	Value at stator/OGV/ESS exit
mid	Value at mid-span
rel	Relative reference frame quantity
<i>x</i>	Axial component
θ	Circumferential component

REFERENCES

- [1] Greitzer, E. M. et al., 2010, "N+3 Aircraft Concept Designs and Trade Studies, Final Report," *NASA Contract Report*, NASA/CR—2010-216794.
- [2] Felder, J. L., Brown, G. V., Kim, H. D. and Chu, J., 2011, "Turboelectric Distributed Propulsion in a Hybrid Wing Body Aircraft," *20th ISABE Conference*, ISABE-2011-1340, Gothenburg.
- [3] Hall, C. A., Schwartz, E. and Hileman, J. I., 2009, "Assessment of Technologies for the Silent Aircraft Initiative," *Journal of Propulsion and Power*, 25(6), pp. 1153-1162.
- [4] Smith, L. H., 1993, "Wake Ingestion Propulsion Benefit," *Journal of Propulsion and Power*, 9(1) pp. 74-82.
- [5] Hall, C. A. and Crichton, D., 2007, "Engine Design Studies for a Silent Aircraft," *Journal of Turbomachinery*, 129(3), pp. 479-487.
- [6] Longley, J. P. and Greitzer, E. M., 1992, "Inlet Distortion Effects in Aircraft Propulsion System Integration," AGARD LS-183, "Steady and Transient Performance Prediction of Gas

Turbine Engines", pp. 6-1–6-18.

- [7] Rabe, D. C., Williams, C. and Hah, C., 1999, "Inlet Flow Distortion and Unsteady Blade Response in a Transonic Axial-Compressor Rotor," *International Symposium on Air Breathing Engines*, ISABE 99-7287.
- [8] Reid, C., 1969, "The Response of Axial Flow Compressors to Intake Flow Distortion," *Proceedings of the Gas Turbine Products and Conference Show, Cleveland, Ohio*, 69-GT-29.
- [9] Greitzer, E. M., Mazzawy, R. S. and Fulkerson, D. A., 1978, "Flow Field Coupling Between Compression System Components in Asymmetric Flow," *Journal of Engineering for Power*, 100(1), pp. 66-72.
- [10] Greitzer, E. M. and Griswold, H. R., 1976, "Compressor-Diffuser Interaction With Circumferential Flow Distortion," *Journal of Mechanical Engineering Science*, 18(1), pp. 25-38.
- [11] Jerez Fidalgo, V., Hall, C. A. and Colin, Y., 2012, "A Study of Fan-Distortion Interaction Within the NASA Rotor 67 Transonic Stage," *Journal of Turbomachinery*, 134(5), p. 051011.
- [12] Yao, J., Gorrell, S. E. and Wadia, A. R., 2010, "High-Fidelity Numerical Analysis of Per-Rev-Rev Type Inlet Distortion Transfer in Multistage Fans," *Journal of Turbomachinery*, 132(4), p. 041014.
- [13] Gunn, E. J., Hall, C. A., Tooze, S. E. and Colin, Y., 2013, "An Experimental Study of Loss Sources in a Fan Operating With Continuous Inlet Stagnation Pressure Distortion," *Journal of Turbomachinery*, 135(5), p. 051002.
- [14] Mistry, C. S. and Pradeep, A. M., 2013, "Investigations on the Effect of Inflow Distortion on the Performance of a High Aspect Ratio, Low Speed Contra Rotating Fan Stage," *Proceedings of ASME Turbo Expo 2013, San Antonio, Texas*, GT2013-94311.
- [15] Dowling, A. P. and Greitzer, E. M., 2007, "The Silent Aircraft Initiative - Overview," *45th AIAA Aerospace Sciences Meeting, Reno, Nevada*, AIAA-2007-0452.
- [16] Madani, V. and Hynes, T. P., 2009, "Boundary Layer Ingesting Intakes: Design and Optimization," *Proceedings of XIX International Symposium on Air Breathing Engines*, ISABE 2009-1346.
- [17] Brandvik, T. and Pullan, G., 2011, "An Accelerated 3D Navier-Stokes Solver for Flows in Turbomachines," *Journal of Turbomachinery*, 133(2) p. 021025.
- [18] Spalart, P. R. and Allmaras, S. R., 1994, "A One-Equation Turbulence Model for Aerodynamic Flows," *La Recherche Aérospatiale*, 1 pp. 5-21.
- [19] Shahpar, S. and Lapworth, L., 2003, "PADRAM: Parametric Design and Rapid Meshing System for Turbomachinery Optimisation," *Proceedings of ASME Turbo Expo 2003*, GT2003-38698.
- [20] Shaw, M. J., Hield, P. and Tucker, P. G., 2013, "The Effect of Inlet Guide Vanes on Inlet Flow Distortion Transfer and Transonic Fan Stability," *Proceedings of ASME Turbo Expo 2013, San Antonio, Texas*, GT2013-94998.
- [21] Korsia, J. J., 2009, "VITAL - European R&D Programme for Greener Aero-Engines," *International Symposium on Air Breathing Engines*, ISABE 2009-1114.
- [22] Florea, R. V., Voytovych, D., Tillman, G., Stucky, M., Shabbir, A., Sharma, O. and Arend, D. J., 2013, "Aerodynamic Analysis of a Boundary-Layer-Ingesting Distortion-Tolerant Fan," *Proceedings of ASME Turbo Expo 2013, San Antonio, Texas*, GT2013-94656.
- [23] Lieblein, S., Schwenk, F. C. and Broderick, R. L., 1953, "Diffusion Factor for Estimating Losses and Limiting Blade Loadings in Axial-Flow-Compressor Blade Elements," *National Advisory Committee for Aeronautics (NACA) Research*

Memorandum, NACA RM E53D01.

- [24] Rowlands, P. A., 2000, "Swept Fan Blade," *United States Patent Number 6,071,077*.
- [25] Denton, J. D., 1993, "Loss Mechanisms in Turbomachines," *Journal of Turbomachinery*, 115(4), pp. 621-656.
- [26] Denton, J. D., 2002, "The Effects of Lean and Sweep on Transonic Fan Performance: A Computational Study," *TASK Quarterly*, 6(1) pp. 7-24.
- [27] Elder, J. W., 1959, "Steady Flow Through Non-Uniform Gauzes of Arbitrary Shape," *Journal of Fluid Mechanics*, 5(3) pp. 355-368.
- [28] Turner, J. T., 1969, "A Computational Method for the Flow Through Non-Uniform Gauzes: the General Two-Dimensional Case," *Journal of Fluid Mechanics*, 36(2) pp. 367-383.
- [29] Livesey, J. L. and Laws, E. M., 1973, "Flow Through Non-Uniform Gauze Screens," *Journal of Fluid Mechanics*, 59(4) pp. 737-743.

APPENDIX: DISTORTION GAUZE DESIGN

The stagnation pressure loss across a gauze, as shown in Fig. 21, is directly proportional to the flow dynamic head at the plane of the gauze [27]:

$$p_{02} - p_{01} = -K \frac{1}{2} \rho V_g^2 \quad (2)$$

The constant of proportionality, K , is a measure of the blockage. If K varies across the gauze, a non-uniform stagnation pressure distribution is imposed on the downstream flow. This principle can be used to redistribute a uniform upstream velocity profile into a non-uniform downstream velocity profile as shown in Fig. 21. In general K is a function of solidity (the fraction of the axial flow area blocked by the gauze), Reynolds number, axial thickness and shape. For most practical purposes the Reynolds number dependence is weak [27] so for a thin, flat gauze, K is a function of solidity only.

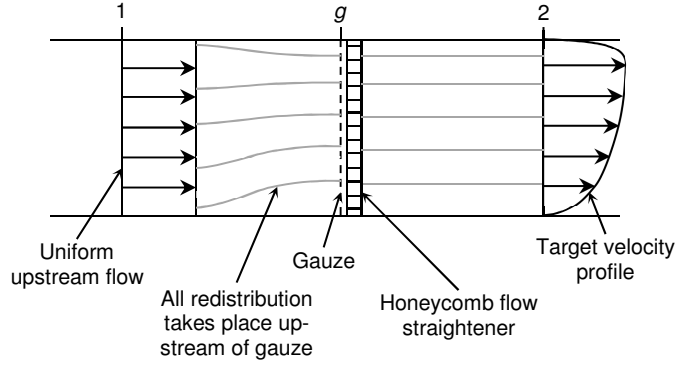


Figure 21: Schematic of the flow through a non-uniform gauze with a coupled flow straightener.

For the general case of an isolated gauze in a duct, Eq. (2) must be solved numerically [28] because flow redistribution occurs gradually both upstream and downstream of the gauze so $V_g(r,\theta) \neq V_2(r,\theta)$. If a flow straightener is placed immediately downstream of the gauze the problem is simplified. The streamlines downstream of the straightener must be straight and parallel so all flow redistribution must take place upstream of the gauze. Hence $V_g(r,\theta) = V_2(r,\theta)$ and p_2 is a constant. This has the important advantage of ensuring that the gauze-induced flow redistribution takes place outside of the mea-

urement domain in the rig and guarantees that the turbomachine sees the correct inlet velocity profile. It also conveniently simplifies the mathematics. Rearranging Eq. (2), noting that $V_g = V_2$ and assuming incompressible flow for simplicity, leads to a simple relationship between the blockage distribution and the target velocity profile:

$$K(r,\theta) = \frac{p_{01} - p_{02}(r,\theta)}{\frac{1}{2} \rho V_2^2(r,\theta)} = \frac{p_{01} - p_2}{\frac{1}{2} \rho V_2^2(r,\theta)} - 1 \quad (3)$$

Where p_{01} is set by the upstream flow field and in most rigs it should be almost uniform. To close this equation the designer must fix values of K and V_2 at one location in the annulus. In practice the authors found that the best approach was to impose a minimum value of K at the known location of maximum V_2 because this corresponds to the most structurally weak part of the gauze. Once these values are fixed, p_2 is a known constant and Eq. (3) is closed.

It is then necessary to obtain a functional relationship between the gauze blockage K and the physical solidity, s . This can be approximated using existing correlations [29] but is best determined experimentally by producing several test pieces of gauze with known solidities and measuring the resulting pressure loss in the relevant rig. Once the required distribution of $s(r,\theta)$ is known it can be interpolated onto a tesselated grid of holes, whose size should be much smaller than the distortion lengthscales of interest. For the BLI rig a hexagonal mesh was chosen; a detail view of the resulting full-annulus gauze is shown in Fig. 22. Simple geometry is used to relate the required solidity value to the local web thickness. Most Computer-Aided Design (CAD) packages are capable of automatically generating a solid body definition of the gauze for manufacture by importing a suitably formatted dataset of the hole centres and sizes.

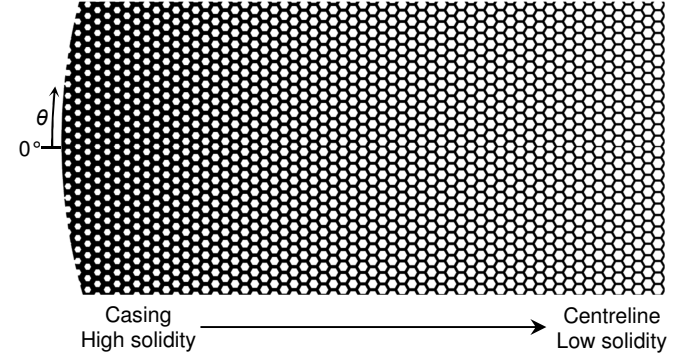


Figure 22: Detail view of the full-annulus distortion gauze for the BLI rig test.